Science of Remote Sensing 11 (2025) 100184

Contents lists available at ScienceDirect

Science of Remote Sensing

journal homepage: www.sciencedirect.com/journal/science-of-remote-sensing

Salinity Indian Ocean Dipole: Another facet of the Indian Ocean Dipole phenomenon from satellite remote sensing

Wei Shi [a,b,*], Menghua Wang [a]

[a] NOAA National Environmental Satellite, Data, and Information Service, Center for Satellite Applications and Research, E/RA3, 5830 University Research Ct., College Park, MD, 20740, USA
[b] CIRA at Colorado State University, Fort Collins, CO, 80523, USA

ARTICLE INFO

Keywords:
Indian Ocean Dipole (IOD)
Salinity IOD
Equatorial Indian Ocean
Positive IOD
Negative IOD
Aquarius mission
Soil Moisture Active Passive (SMAP) mission

ABSTRACT

Using satellite-measured sea surface salinity (SSS) from the Aquarius and Soil Moisture Active Passive (SMAP) missions since 2011, we show that SSS in the Equatorial Indian Ocean (EIO) experienced dipolar changes in the well-defined east EIO and west EIO regions during the Indian Ocean Dipole (IOD) events. Similar to the concepts of dipole mode Index (DMI) and biological dipole mode index (BDMI), a salinity dipole mode index (SDMI) is proposed using the same definition for the east and west IOD zones. The results show that the salinity IOD in this study is in general co-located and co-incidental with the sea surface temperature (SST) IOD and biological IOD in previous studies. In the positive IOD event in 2019, the SSS anomaly was >1 psu for most of the east IOD zone, while the average SSS in the west IOD zone was ~0.2–0.3 psu lower than the climatology monthly SSS. The reversed SSS dipolar variability in the EIO was also found during the 2022 negative IOD event. The SSS anomaly difference between the east IOD zone and west IOD zone shows the same variation as the SST-based DMI and chlorophyll-a (Chl-a)-based BDMI. The in situ measurements show that, in the 2019 positive IOD event, the significant IOD-driven salinity change reached water depths at ~70–80 m and ~50 m in the east and the west IOD zones, respectively. Results also reveal that the salinity IOD is not only driven by the various ocean processes (e.g., upwelling, downwelling, propagation of the planetary waves, etc.), which are also the main driving forcing for the SST IOD and biological IOD, but also the precipitation and evaporation in the two IOD zones, especially in the west IOD zone. In addition to the traditional SST IOD and recently proposed biological IOD, the salinity IOD indeed features another facet of the entire IOD phenomenon.

1. Introduction

Indian Ocean Dipole (IOD) in the Equatorial Indian Ocean (EIO) is an ocean-atmosphere phenomenon with dipolar ocean variability in the east and west EIO regions. Traditionally, the IOD is referred as the dipolar sea surface temperature (SST) anomaly in the east and west EIO regions (Saji et al., 1999; Webster et al., 1999). The dipolar SST anomaly in the east and west EIO zones is driven by intra-seasonal oscillation of wind along the west Sumatra Coast (Vinayachandran et al., 1999, 2002) due to the anomalous inter-hemisphere pressure gradient (IHPG) (Zhang et al., 2021) and the westward propagation of the upwelling Rossby waves (Vinayachandran et al., 2002). There are some clear linkages and interactions between the IOD event in the Indian Ocean and the El Niño Southern Oscillation (ENSO) activities in the Equatorial Pacific Ocean (Behera and Yamagata, 2003; Doi et al., 2020; Luo et al., 2010). It is also found that there was increased frequency of extreme IOD events and increased occurrences of early IOD events due to greenhouse warming (Cai et al., 2014; Sun et al., 2022b; Wang et al., 2024).

The IOD event significantly impacts the global atmosphere and ocean variability, especially in the Indian Ocean. In addition to the linkage and interaction between the IOD event and ENSO activities, the Indian Summer Monsoon is closely associated with the IOD event, showing above-normal (below-normal) monsoon rainfall over the Indian sub-continent during a positive (negative) IOD event (Ashok et al., 2001; Prajeesh et al., 2022; Ratna et al., 2021). The IOD-associated SST anomaly in the west EIO accompanied with the excessively strong short rains in the coastal East Africa (Black et al., 2003) and Sri Lanka (Zubair et al., 2003). The precipitation patterns in the southeast Indian Ocean

* Corresponding author. NOAA National Environmental Satellite, Data, and Information Service, Center for Satellite Applications and Research, E/RA3, 5830 University Research Ct., College Park, MD, 20740, USA.
E-mail address: wei.1.shi@noaa.gov (W. Shi).

https://doi.org/10.1016/j.srs.2024.100184
Received 17 October 2024; Received in revised form 21 November 2024; Accepted 9 December 2024
Available online 10 December 2024

(SEIO) between the positive IOD (p-IOD) and negative IOD (n-IOD) are asymmetric (Gao et al., 2014). The wildfires in Indonesia and severe drought in the southeast Australia caused by the rainfall deficit and substantial reductions were also driven by the p-IOD events (Abram et al., 2003; Cai et al., 2009; Ummenhofer et al., 2009). Interannual upper ocean and subsurface variability in the tropical Indian Ocean is also significantly impacted by the IOD event (Feng et al., 2001; Rao et al., 2002). In fact, ~12% of the SST variability in the tropical Indian Ocean was attributed to the IOD event (Saji et al., 1999). The interannual variability of the barrier layer is closely related to the IOD with the IOD leading the barrier layer by about one month (Qiu et al., 2012). In addition to the physical variability driven by the IOD event, chlorophyll-a (Chl-a) anomaly, phytoplankton bloom, enhanced phytoplankton biomass caused by the IOD event have been reported in the various Indian Ocean regions (Currie et al., 2013; Iskandar et al., 2009; Thushara and Vinayachandran, 2020).

Due to the sparse ocean salinity data before the space-based SSS missions such as Aquarius (Le Vine et al., 2007) or Soil Moisture Active Passive (SMAP) (O'Neill et al., 2010) in 2010s, most of our knowledge about SSS in the Indian Ocean was from the in situ measurements and ocean modelling studies. The impact of IOD on the salinity budget in the EIO is significant (Zhang et al., 2013). Large interannual sea surface salinity (SSS) variations with two zonal bands appear in the Indian Ocean only during IOD years in the EIO (Vinayachandran and Nanjundiah, 2009). Asymmetric response of SSS to the extreme positive and negative IOD events was found in the southern Tropical Indian Ocean (Sun et al., 2022a). The Tropical Indian Ocean shows the contrasting interannual SSS variability with anomalously low-salinity in the Central Equatorial Indian Ocean and high-salinity in the southeastern Tropical Indian Ocean during the IOD event (Zhang et al., 2016). In the negative IOD event, enhanced SSS in the southwestern tropical Indian Ocean is attributed to the horizontal advection of the high salinity waters, decreased precipitation, and shoaling thermocline driven by the upwelling Rossby waves (Sun et al., 2019).

To characterize and quantify the IOD activities, the Dipole Mode Index (DMI) as the SST anomaly (SSTA) difference between the west IOD zone (50°E–70°E, 10°S–10°N) and the east IOD zone (90°E–110°E, 10°S–0°N) was proposed (Saji et al., 1999). The p-IOD is featured with SST cooling, lower sea level, and shallow thermocline in the east IOD pole as well as the warmer-than-normal SST and deepening thermocline in the west IOD pole, and vice versa for the n-IOD event. A positive biological IOD in 2019 was identified with enhanced Chl-a in the east EIO and decreased Chl-a in the west EIO (Shi and Wang, 2021). Using the same concept to define DMI with SSTA, the Biological Dipole Mode Index (BDMI) was proposed with the same definition of the east and west IOD zones (Shi and Wang, 2022b). Both the DMI and BDMI can characterize the IOD activities well, and BDMI reflects both the physical and biological aspects of the IOD events (Shi and Wang, 2022b).

Even though IOD was initially identified and proposed as the dipolar change of SST in the east and west EIO zones, IOD actually is a multifacet event of interannual fluctuations of the atmosphere and ocean in the EIO. These aspects of the IOD in a broad sense include not only the SST IOD but also biological IOD. Numerous studies have shown the SSS variability when the IOD event occurred, and some even were described as the salinity dipole (Durand et al., 2013; Kido et al., 2019; Li et al., 2016; Sun et al., 2022a; Zhang et al., 2016). However, none of these studies ever focused on the two IOD zones, which are well defined and accepted for the IOD events (Saji et al., 1999; Shi and Wang, 2021; Webster et al., 1999). In this study, we analyze the satellite observations of SSS from the Aquarius and SMAP since early 2010s, characterize and quantify the salinity IOD in the EIO as another facet of the IOD phenomenon. Correspondingly, the concept of the salinity IOD, which is consistent with the SST-based IOD and Chl-a-based BIOD, is proposed. The in situ measurements in the east and west IOD zones are also explored in order to conduct a comprehensive evaluation for understanding of the effect of the salinity IOD in the water column and the mechanism that drives the salinity IOD in the EIO region.

2. Data and methods

In this study, satellite-derived SSS from the Aquarius and SMAP missions, and DMI and BDMI data are used to characterize the interannual variability of the salinity in the EIO and examine the consistence of the dipolar salinity changes with the SST IOD and biological IOD in the two IOD zones. The vertical salinity profiles and driving mechanism for the salinity IOD are also explored with the in situ measurements at two stations in the east and west IOD zones.

In this study, the Visible Infrared Imaging Radiometer Suite (VIIRS) global ocean color product data are available at the NOAA CoastWatch (https://coastwatch.noaa.gov/). The in situ wind, precipitation, evaporation, ocean temperature and salinity data were obtained from NOAA Physical Science Laboratory (https://psl.noaa.gov/). The satellite SSS data were acquired from Physical Oceanography Distributed Active Archive Center (PODAAC) of NASA Jet Propulsion Laboratory (JPL) (https://podaac.jpl.nasa.gov/).

2.1. SSS data from Aquarius and SMAP

Satellite SSS measurements are based on L-band microwave sensitivity to water salinity (Fore et al., 2016). The satellite SSS data with spatial resolution of 150-km and a repeat cycle of seven days were made with Aquarius onboard the Argentine SAC-D spacecraft between mid-2011 and mid-2015 (Le Vine et al., 2007). The SMAP has been providing the global soil moisture product since early 2015 at 685-km altitude with an 8-day repeat cycle. In addition, the onboard radar and radiometer also provide SSS observations with a resolution on 25-km swath grid for Level-2 data, and a resolution of $0.25^\circ \times 0.25^\circ$ for Level-3 data.

Comparison between the monthly SMAP SSS retrievals and the objectively interpolated (OI) gridded monthly Argo datasets shows that the SMAP SSS data have an accuracy of ~0.2 psu in the tropics. Even though the Aquarius SSS and SMAP SSS have different spatial resolution, the difference of the global monthly Aquarius SSS and SMAP SSS in April and May 2015 is insignificant with a mean of 0.013 psu and a median of 0.014 psu, respectively. This demonstrates that these two datasets can be combined to study the SSS variability in the EIO.

Since the SST IOD and BIOD are both characterized as the SST and Chl-a anomalies from their climatology monthly SST and Chl-a in the EIO, respectively, the monthly SSS measurements from the Aquarius (September 2011–May 2015) and SMAP (April 2015–June 2023) are used to compute the monthly SSS climatology in the EIO. Specifically, the climatology SSS value at a location in a certain month is calculated as the mean SSS value in the corresponding months from both the Aquarius and SMAP between 2011 and 2023.

Following the monthly climatology SSS in the EIO region, the monthly SSS anomaly (SSSA) is calculated as the difference between the satellite monthly SSS and the corresponding monthly climatology SSS. Using the mean SSSA values in the east and west IOD zones, we can then derive the SSSA difference between the east and west IOD zones. The temporal variation of the SSSA difference consequently can be assessed and provide us an insight about the SSS IOD event, and its relation to the SST IOD and BIOD.

2.2. The DMI and BDMI data

As the parameter for measuring the SST IOD, DMI, which is the monthly SSTA differences between the east and west IOD zones, are periodically computed and archived at NOAA Physical Science Laboratory (https://psl.noaa.gov/gcos_wgsp/Timeseries/DMI/). The SSTA at the east and west IOD zones are averaged correspondingly after subtracting the 1981–2010 climatology values from each month from the monthly Hadley Centre Global Sea Ice and SST (HadISST1.1) (Rayner

et al., 2003).

As the parameter for the BIOD, $BDMI^{(Ratio)}$ (Shi and Wang, 2022b) is computed using global Chl-a data (Wang and Son, 2016) derived from VIIRS onboard the Suomi National Polar-orbiting Partnership (SNPP) (Goldberg et al., 2013; Wang et al., 2013) from 2012 to early 2023 at the NOAA Ocean Color Science Team (https://www.star.nesdis.noaa.gov/sod/mecb/color/). In fact, global gap-free ocean color products (including Chl-a) are highly useful (Liu & Wang, 2018, 2019, 2022) and available from NOAA CoastWatch. Following the procedure in Shi and Wang (2022b), monthly climatology Chl-a in the EIO were derived from VIIRS-SNPP observations. The Chl-a anomalies as the ratio (or relative difference) between the monthly Chl-a and the corresponding monthly climatology Chl-a were then computed, and eventually the $BDMI^{(Ratio)}$ in each month is calculated as the difference of averages of the Chl-a ratio anomalies $BDMI^{(Ratio)}$-E in the east IOD zone and $BDMI^{(Ratio)}$-W in the west IOD zone.

In recent years, there occurred one extreme p-IOD event in 2019 (Shi and Wang, 2021) and a notable n-IOD event in 2022 (Shi and Wang, 2024). Specifically, the DMI reached +0.964 °C in October 2019, and DMI was −0.691 °C in October 2022. The BDMIs also show positive BIOD with BDMIs at 0.829 and 1.028 in October and November 2019 (Shi and Wang, 2022a), respectively, and negative BIOD with BDMI of −0.347 in October 2022 (Shi and Wang, 2024). In this study, the SSS anomalies and its dipolar changes in the EIO in the two p-IOD and n-IOD periods are characterized/quantified and used as examples to show the salinity IOD activity in the EIO region. In addition, some detailed comparisons of the salinity IOD features with those from the corresponding SST IOD and BIOD, in terms of timing and intensity, are provided.

2.3. The RAMA data and World Ocean Atlas 2018 (WOA18)

Research Moored Array for African-Asian-Australian Monsoon Analysis and Prediction (RAMA) are the collective meteorological and oceanographic data in the Indian Ocean since 2004 (https://www.pmel.noaa.gov/gtmba/pmel-theme/indian-ocean-rama). Of the 39 observation sites in the Indian Ocean, one is located at [95°E, 5°S] within the east IOD zone (station A in Fig. 1a), and another is located at [57°E, 4°S] in the west IOD zone (station B in Fig. 1a). In this study, the ocean temperature and salinity, wind speed, 20 °C isotherm depth, precipitation, and evaporation at these two stations are used to further explore the driving forces for the salinity variability in the east and west IOD zones.

It is also noted that the in situ measurements at these two stations were intermittent, and not available all the time. At station A, the RAMA data in 2018–2020 are available to cover the 2019 p-IOD, and no measurements were made in the period of the 2022 n-IOD event. At station B, the temperature and salinity profile data between late 2018 and 2020 are available for the 2019 p-IOD event, and the wind, rainfall and evaporation data are partially available in 2018–2020. There are also no data at station B in 2022 for the 2022 n-IOD event. Corresponding to the data availability at stations A and B, only the RAMA in situ measurements in 2018–2020 are used to study salinity change in the water column and the driving forcing for the positive salinity IOD in 2019.

As the world's largest publicly available collection of surface and subsurface ocean data, World Ocean Atlas 2018 (WOA18) (Boyer et al., 2005) provide information of the temperature and salinity profiles and the climatology monthly changes of the ocean and atmosphere parameters at stations A and B. These climatology monthly variations are also used as references and baselines to further evaluate the in situ measured changes of the relevant ocean and atmosphere parameters in 2018–2020 to address the driving forcing for the 2019 salinity IOD event.

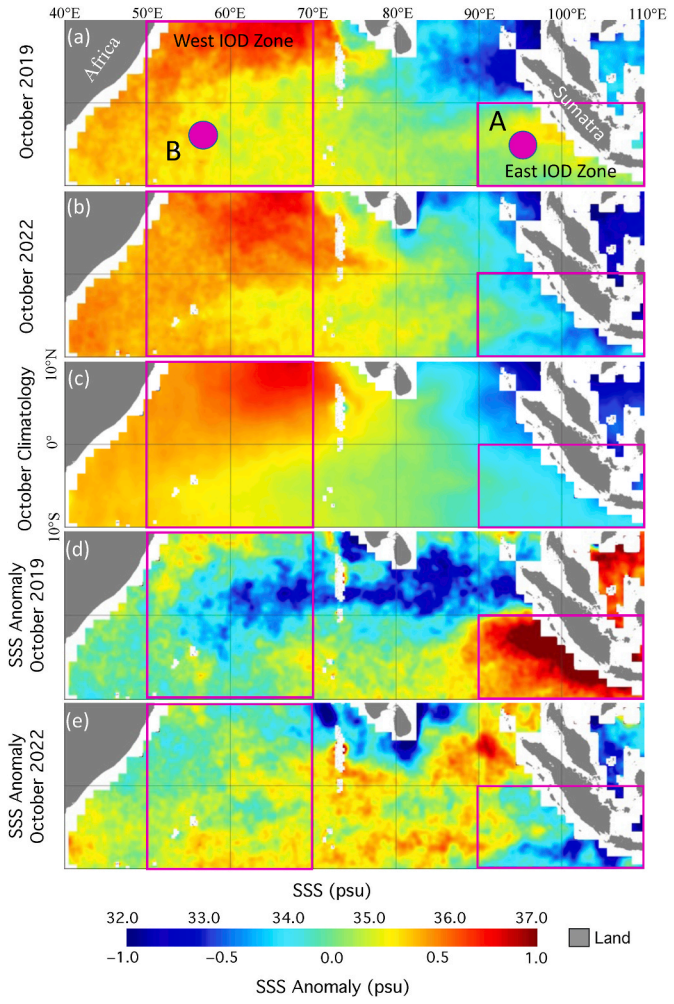

Fig. 1. (a) SSS in October 2019, (b) SSS in October 2022, (c) SSS climatology in October, (d) SSSA in October 2019, and (e) SSSA in October 2022. Note that the east IOD zone (90°E–110°E, 10°S–0°N) and west IOD zone (50°E–70°E, 10°S–10°N) are marked in each panel, and the locations for in situ measurements at stations A (95°E, 5°S) and B (57°E, 4°S) are also marked in panel (a).

3. Results

3.1. The 2019 positive and 2022 negative SSS IOD events

Following the positive SST IOD and BIOD in 2019 and negative SST IOD and BIOD in 2022 as identified in DMI and BDMI results, satellite-derived SSS images in October 2019 and October 2022 in the EIO region are examined. As a reference for SSS in the EIO in October (Fig. 1c), the climatology SSS generally show a decreasing trend from the west to east EIO region. Specifically, SSS were in the range of 35.5–36.5 psu in the west IOD zone, while SSS were at 33.5–34.5 psu in the east IOD zone.

In October 2019 for the p-IOD, broad notable SSS increase can be found in the east IOD zone (Fig. 1a) with SSS ~35 psu. In the offshore region of Sumatra, SSS even reached 35.5–36.0 psu. In the west IOD zone, the coverage of high SSS over 36.0 psu decreased significantly in October 2019 in comparison to the coverage from the SSS climatology in October (Fig. 1c). In the northeastern EIO region between Sri Lanka and Sumatra, SSS in October 2019 also showed significant drop from the climatology SSS in October.

In October 2022 for the n-IOD, the SSS map (Fig. 1b) was apparently different from that in October 2019 (Fig. 1a). In comparison with the SSS climatology in October (Fig. 1c), SSS in the east IOD zone showed overall decrease even though enhanced SSS indeed existed in the farther

offshore region of Sumatra. In the west IOD zone, SSS in the northern part were similar to the climatology SSS, and moderate increase of SSS was found in the southern part of the west IOD zone.

The SSSA maps in the EIO region during the p-IOD in October 2019 (Fig. 1d) and during n-IOD in October 2022 (Fig. 1e) clearly showed the dipolar SSS variability in the east and west EIO regions. Fig. 1d shows that SSSA reached over ~1 psu in a large portion of the east IOD zone. A band of negative SSSA north of the equator extended from 60°E to 95°E. In the west IOD zone, positive SSSA were located in the northwestern and southern parts of this region. The spatial pattern of SSSA in October 2022 (Fig. 1e) showed that the negative SSS were mainly located in the southern east IOD zone. A broad SSS increase could be found in the entire west IOD zone. Most of the enhanced SSS increase of ~0.3–0.4 psu were located in the southern west IOD zone.

3.2. The SSS variability in the east and west IOD zones

For both the SST IOD and biological IOD, contrasting dipolar changes occurred in the east and west EIO regions. Fig. 2a and b shows the temporal variations of the average salinity in the east and west IOD zone, respectively. The climatology monthly SSS varies between 33.74 psu and 33.99 psu in the east IOD zone, while it ranges from 35.26 to 35.59 psu in the west IOD zone. For the p-IOD in 2019, the average SSS in the east IOD zone spiked to 34.49, 34.64, and 34.66 psu in October, November, and December (Fig. 2a), respectively. In comparison, decreased SSS lagged about 2–3 months in the west IOD zone (Fig. 2b). The average SSS were 35.36, 35.20, and 35.10 psu in December 2019, January 2020, and February 2020, respectively, while the corresponding monthly climatology average SSS for these three months are 35.54, 35.45, and 35.40 psu, respectively.

In the 2022 n-IOD event, the average SSS in the east IOD zone was 33.55 psu in October 2022 in comparison to the October climatology value of 33.88 psu (Fig. 2a). On the other hand, the peak SSS in the west IOD zone lagged about one month and occurred at 35.81 psu in November 2022 (Fig. 2b). It is also noted that a negative salinity IOD happened in the summer 2016 with depressed SSS in the east IOD zone (Fig. 2a) and near-normal SSS in the west IOD zone (Fig. 2b).

Similar to the SSTA in the west pole region (50°E–70°E, 10°S–10°N) and east pole region (90°E–110°E, 10°S–0°N) that define the DMI (Saji et al., 1999) and BDMI (Shi and Wang, 2022b), we choose the same east and west IOD zones to define the Salinity Dipole Mode Index (SDMI) to characterize and quantify the SSS variability in the EIO, i.e.,

$$\mathrm{SDMI} = \mathrm{Mean}\left[SSSA^{(E)}(x,y)\right] - \mathrm{Mean}\left[SSSA^{(W)}(x,y)\right] \quad (1)$$

where SDMI represents the SSS anomaly difference between these two IOD zones, and Mean$[SSSA^{(E)}(x, y)]$ and Mean$[SSSA^{(W)}(x, y)]$ are computed as the mathematical mean values of the corresponding differences between the monthly SSS and the climatology monthly SSS for all pixels in the east and west IOD zones. Fig. 2c shows SDMI in these two zones. Indeed, the SSSA difference reached ~ +1.0 psu in late 2019 during the p-IOD event. In contrast, it was ~ −0.4 psu in the 2022 n-IOD event. In 2016, the difference of SSSA also dropped to the same level as that in 2022.

Fig. 2d shows the consistence and coincidence of the DMI and BDMI with SDMI as shown in Fig. 2c between 2011 and 2022. Even though there exist some minor phase differences, the DMI, BDMI, and SDMI all show the same dipolar variability in the EIO. Positive DMI, BDMI, and SDMI occurred during the p-IOD in 2019, and negative DMI, BDMI, and SDMI were identified during the 2022 n-IOD. In another n-IOD event in 2016 (Lu et al., 2018), DMI, BDMI, and SSSA differences also showed the same features as those in the 2022 n-IOD event.

We further characterized SSSA in the east and west EIO regions. The longitudinal averages of SSSA in the east and west IOD zones were computed in the period between 2018 and 2023 (Fig. 3). In the east IOD zone, SSSA clearly showed significant enhancement across the equator–5°S in the autumn 2019 (Fig. 3a). In late 2019 and early 2020, the positive SSSA were mainly located in the southern part of this region. Indeed, SSSA reached > ~1.0 psu between 1°S and 3.5°S in September, October, and November 2019.

In the west IOD zone, significantly negative SSSA were observed from late autumn of 2019 to spring of 2020 (Fig. 3b). The negative SSSA pattern in the west IOD zone (Fig. 3b) appeared about 2–3 months later than the positive SSSA pattern in the east IOD zone (Fig. 3a). In the east IOD zone, the highest SSSA occurred in October and November 2019, while extreme negative SSSA were in January 2020 in the west IOD zone. In late 2019, the pattern with negative SSSA ~ −0.5 psu covered the region of 10°N–7.5°S in the west IOD zone. In early 2020, the

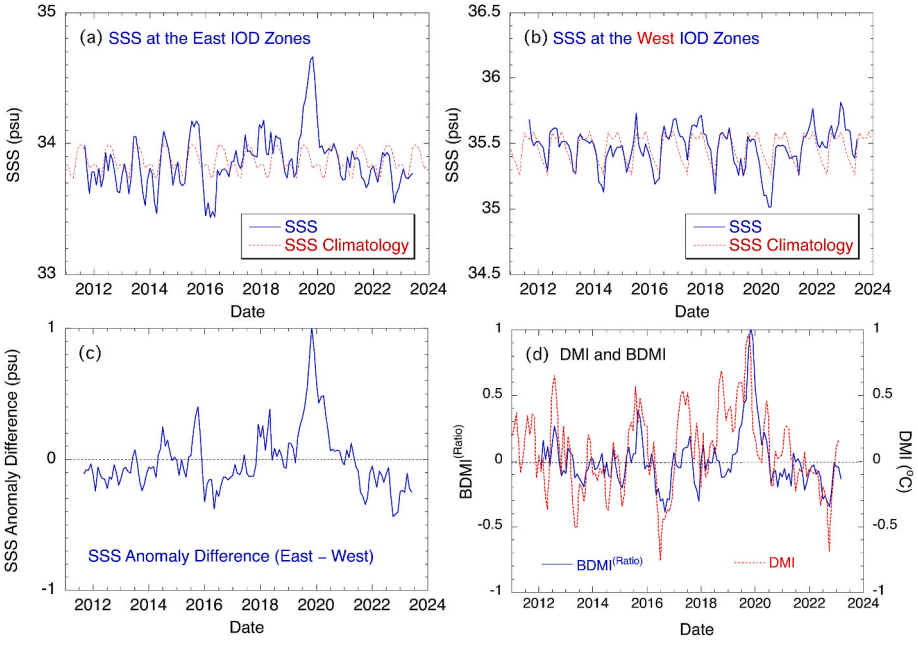

Fig. 2. Time series between 2011 and 2023 for (a) average SSS with embedded climatology monthly SSS in the east IOD zone, (b) average SSS with embedded climatology monthly SSS in the west IOD zone, (c) SSSA difference between the east IOD zone and west IOD zone, and (d) BDMI and DMI.

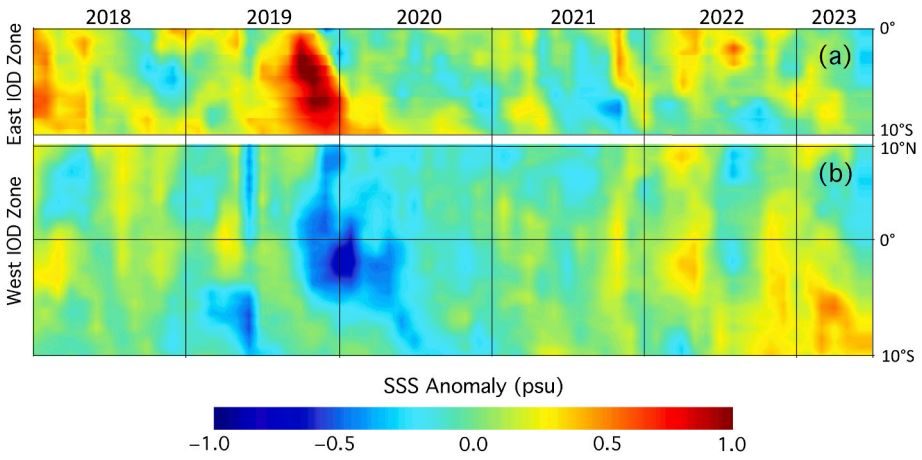

Fig. 3. Longitudinal average SSSA between January 2018 and June 2023 in (a) the east IOD zone and (b) the west IOD zone.

negative SSSA pattern was mainly located in equator−5°S.

As shown in Fig. 2c, the negative SSS IOD in 2022 was moderate in comparison to the extreme positive SSS dipole in 2019. In the east IOD zone, the negative SSSA of ~ −0.3 psu was confined to south of 3°S, and only lasted until the end of 2019. This agrees with SSSA images in Fig. 1e and average SSS in Fig. 2a. In the west IOD zone, the positive SSSA (Fig. 3b) started in late 2019, about one month later than the negative SSSA pattern (Fig. 3a). The positive SSSA pattern with SSSA ~0.3–0.6 psu mainly stretched from 5°S−10°S. The evolutions of the longitudinal average SSSA in the east and west IOD zones show that the magnitudes, locations, spatial patterns, and coverages of SSSA in the two zones actually varied and were event-specific even though the positive and negative dipolar variability of SSS indeed occurred in the EIO region in 2019 and 2022.

3.3. *Dipolar salinity profiles and driving mechanism for the salinity IOD*

3.3.1. *Dipolar salinity profiles at stations A and B*

Figs. 1–3 show the dipolar SSS variability in the EIO. The RAMA station A in the east IOD zone and RAMA station B in the west IOD zone provide us an opportunity to study the dipolar salinity variability in the water column in the east and west IOD zones even though the in situ measurements only covered the 2019 positive salinity IOD event. On the other hand, other parameters such as the temperature profiles, 20 °C isotherm depths, wind speeds, precipitations and evaporations also provide a rare chance to explore the mechanism that drives the salinity IOD in the EIO.

Since all the ocean and atmosphere processes that impact the salinity dipolar variability in the EIO eventually lead to the changes of the temperature and salinity profiles at station A in the east IOD zone and station B in the west IOD zone, it is essential to understand the vertical distributions of the climatology temperature and salinity and their seasonal variations at these two stations. Fig. 4 shows the salinity profiles at stations A (Fig. 4a) and B (Fig. 4b) and temperature profiles at stations A (Fig. 4c) and B (Fig. 4d) from the WOA18 climatology.

The salinity and temperature profiles at stations A and B are notably different in terms of both magnitudes and the vertical distributions. At station A, the depth with almost uniform temperature is ~50–60 m

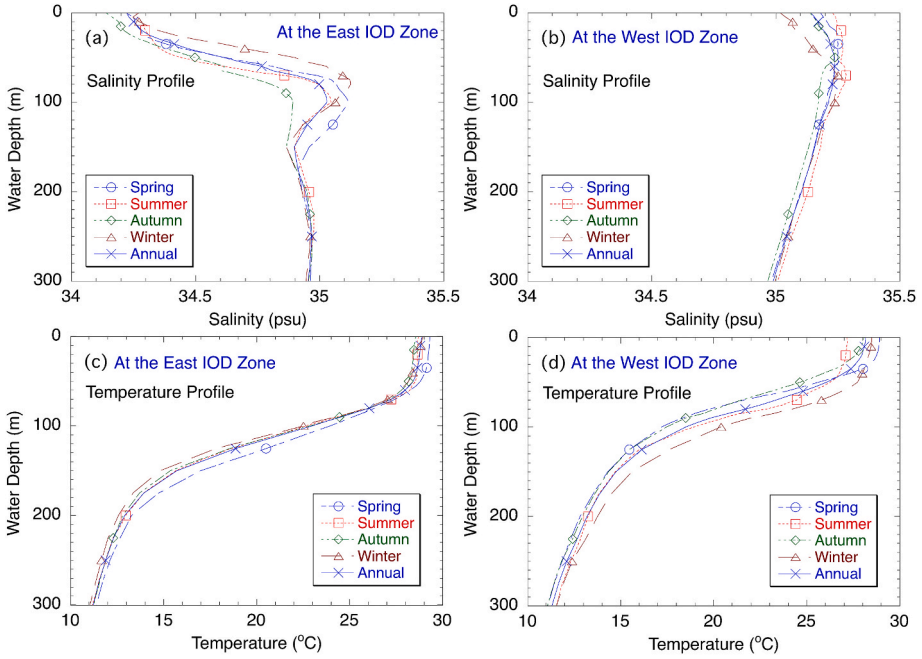

Fig. 4. The WOA18 climatology seasonal and annual mean profiles in the upper 300 m for (a) salinity at station A, (b) salinity at station B, (c) temperature at station A, and (d) temperature at station B.

(Fig. 4c), while the salinity increases from 34.2 psu at sea surface to > 35.0 psu at water depth of ~80 m (Fig. 4a). At station B, the layer with quasi-uniform temperature is only approximately 10 m (Fig. 4d), and the salinity only increases by 0.1 psu from the surface to 30–40 m (Fig. 4b). In comparison to salinity at station A, the vertical variation of salinity at station B is much less significant. The seasonal changes of salinity at stations A and B are also different. At station A, the seasonal high salinity occurs in the boreal winter season and seasonal low salinity in the autumn. In contrast, salinity reaches peak in the summer season and its minimum in the winter season (Fig. 4b). The WOA18 annual and seasonal temperature and salinity profiles provide us the reference and baseline information in order to better understand the salinity variability during the 2019 p-IOD in the EIO region.

Fig. 5 shows the salinity and temperature variability at stations A and B in the period of 2018–2020. Note that there were no measurements of temperature and salinity between January and November 2018 at station B, and salinity was only measured in the upper 100 m depth. At station A, the enhanced salinity >35.0 psu can be observed to reach 100 m in late 2019 (Fig. 5a). The salinity in the upper 70 m was <34.0 psu in the same period in 2018 and 2020. As shown in Fig. 4a, the minimum salinity normally occurred in the autumn season. However, salinity in the autumn of 2019 was featured with the highest salinity in the entire year. The enhancement of salinity at station A in late 2019 came with the shoaling thermocline from the summer of 2019 (Fig. 5c). The enhanced salinity and shoaling thermocline at station A in 2019 were both attributed to the stronger coastal upwelling along the west Sumatra and the offshore advection of the upwelling water (Shi and Wang, 2021).

At station B, the salinity in the upper 5–10 m was featured with <34.0 psu waters from late 2019 to mid-2020 (Fig. 5b). This was significantly lower than the climatology salinity at station B as shown in Fig. 4b. On the other hand, salinity in the water column of upper 50 m also depressed at 34.5 psu between late 2019 and spring 2020. The timing of the depressed salinity was coincident with the deepening of the thermocline (Fig. 5d). The salinity profiles between 2018 and 2020 showed that the 2019 salinity dipole not only occurred at the surface (Figs. 1–3), but also penetrated to over 50 m at both stations A and B. The lowest salinity in the water column at station B occurred in early 2020 (Fig. 6b), this also lagged the enhanced salinity at station A for a couple of months.

3.3.2. Ocean and atmospheric parameters at stations A and B

Fig. 6 further show the ocean and atmospheric parameters and their possible impacts on salinity at stations A and B from 2018 to 2020. As a parameter for thermocline depth for many ocean processes such as the upwelling, downwelling, and propagation of the Earth planetary waves, the 20 °C isothermal depth at station A shows that it started to deviate from the climatology 20 °C isothermal depth and shoaled at 70 m in October 2019 (Fig. 6a). In contrast, the climatology 20 °C isothermal depth is 120 m. Fig. 6c shows the southeasterly wind strengthened in the same period. The salinity profile at station A (Fig. 4a) displays that salinity increased significantly from the surface to 100 m depth. Shi and Wang (2021) show that anomalous alongshore winds off the west Sumatra caused stronger upwelling and brought up the high salinity and nutrient deep ocean waters to the ocean surface. The in situ measurements of the 20 °C isotherm (Fig. 6a) and wind speed (Fig. 6c) at station A agree well with the results in that study (Shi and Wang, 2021). The impact of the strengthened upwelling and advection of the upwelling water not only affected the SSS as shown in Figs. 1d, 2a and 3a, but also the salinity at the upper 100 m depth (Fig. 5a) in the 2019 p-IOD period.

The salinity budget in the EIO is not only affected by the ocean processes, but also by the atmospheric processes such as the precipitation (P), evaporation (E), and net freshwater gain P-E. Fig. 6e shows the precipitation rate and Fig. 6g is the evaporation rate at station A between 2018 and 2020. Clearly, the evaporation rate increased with the strengthened wind from spring to autumn 2019 (Fig. 6c). There was almost no precipitation in autumn 2019. In comparison, the climatology precipitation rate is ~0.4–0.45 mm h^{-1}. The precipitation measurements during the 2019 p-IOD agreed with the dry air and severe drought in that region during a p-IOD (Cai et al., 2009; Ummenhofer et al., 2009). The salinity and temperature variability (Fig. 5a and c), the 20 °C isothermal depth (Fig. 6a), and wind speed (Fig. 6c) at station A coincided with each other during the 2019 p-IOD. This demonstrates that the ocean processes such as the wind-driven upwelling and advection of the upwelling water were not only the driver for the biological variability (Shi and Wang, 2021), but also for the salinity variability in the east IOD zone during the 2019 p-IOD. On the other hand, we have not found any evidence that the salinity variability was notably affected by the precipitation and evaporation during the 2019 p-IOP even though the anomalously low precipitation and enhanced evaporation indeed occurred and tended to lead to the increase of the salinity, especially SSS in the east IOD zone. This could be attributed to the thick mixed-layer

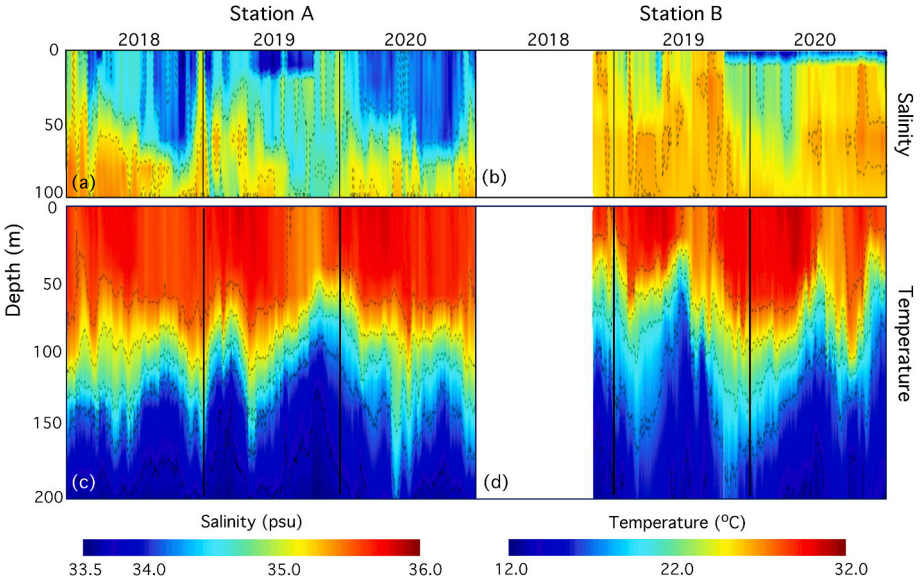

Fig. 5. Temporal variations between January 2018 and December 2020 for (a) salinity in the upper 100 m at station A, (b) salinity in the upper 100 m at station B, (c) temperature in the upper 200 m at station A, and (d) temperature in the upper 200 m at station B.

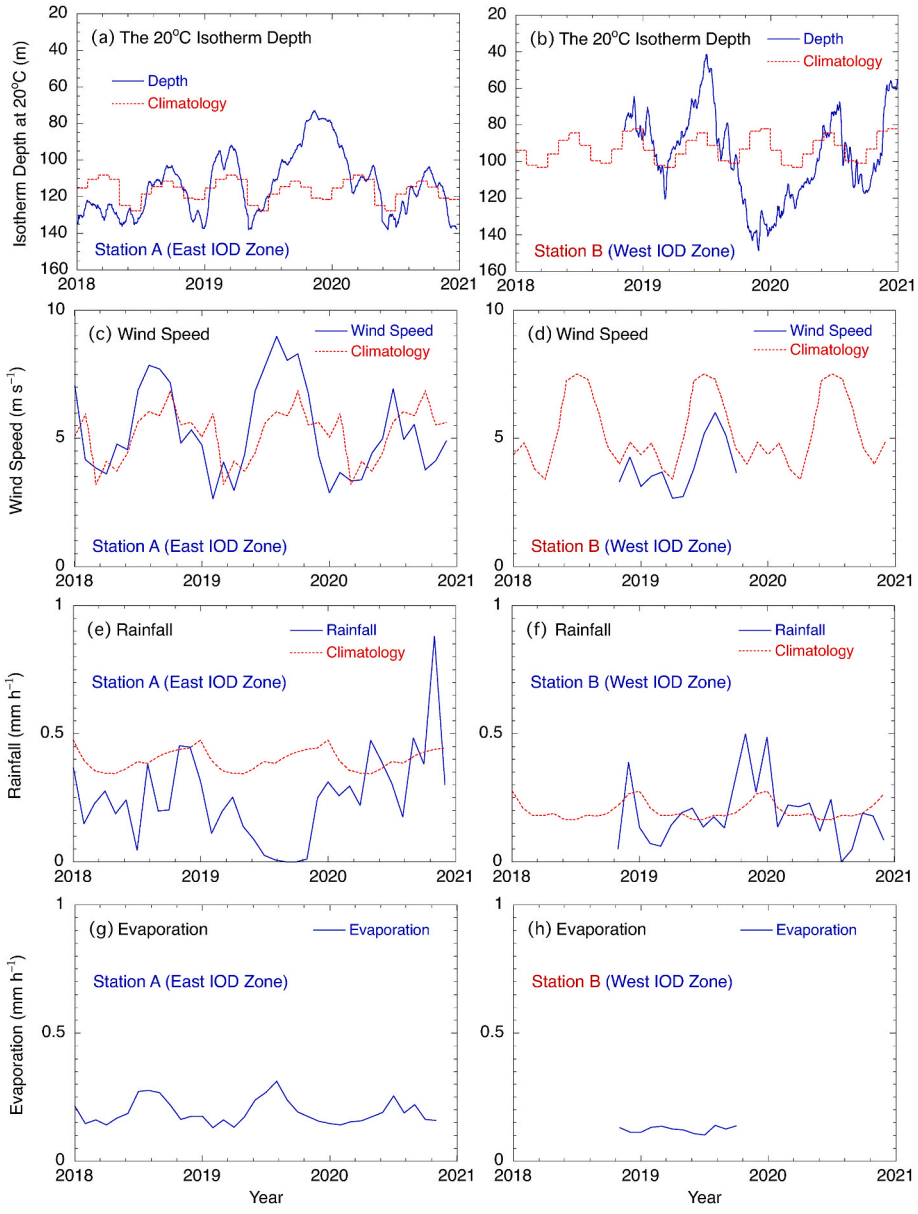

Fig. 6. Temporal variations between 2018 and 2020 for (a) the 20 °C isotherm depth at station A, (b) the 20 °C isotherm depth at station B, (c) wind speed at station A, (d) wind speed at station B, (e) precipitation at station A, (f) precipitation at station B, (g) evaporation at station A, and (h) evaporation at station B. Note that red dash lines in plots 6a–6f represent the WOA18 monthly climatology changes at stations A and B for each corresponding parameter.

and enhanced vertical mixing, entrainment and upwelling at station A during the 2019 p-IOD event.

Contrasting to the measurements at station A, the in situ measurements at station B show that the salinity or temperature variability (Fig. 5b and d) and the deepening 20 °C isotherm (Fig. 6b) were in phase with each other in late 2019. In late 2019, the 20 °C isothermal depth was >50 m deeper than the climatology 20 °C isotherm depth. It lagged the occurrence of shoaling 20 °C isotherm at station A for about 1–2 months. The wind speed at station B (Fig. 6d) was weaker between January and September 2019. The precipitation measurements were close to the climatology before autumn 2019 (Fig. 6f). Starting in October 2019, the precipitation at station B reached >0.5 mm h^{-1}, and the high-than-normal precipitation lasted until early 2020. The evaporation was stable at ~0.1 mm h^{-1} before autumn 2019. In fact, the anomalous precipitation since autumn 2019 timed well with the fresher surface layer as shown in Fig. 5b.

The in situ measurements at station B provide further evidence that the deepening thermocline due to the downwelling, Ekman pumping, and surface water convergence not only caused the lower Chl-a in the 2019 p-IOD event (Shi and Wang, 2021), but also led to the decrease of salinity in the upper 70 m waters. Since the mixed-layer depth at station B was shallow (Fig. 4d), the excessive P-E could significantly affect SSS in the region. The net freshwater gain P-E of 0.4 mm h^{-1} in October 2019 as suggested in Fig. 6f and h was estimated to cause a salinity drop of ~1.0 psu in a month in a 10 m surface mixed-layer, assuming there were no vertical and lateral salt exchanges at this station. This indeed implies that the P-E in the west IOD zone was an indispensable forcing for the SSS variability during the 2019 p-IOD event.

3.3.3. *Driving forcing for dipolar salinity change in the east and west IOD zones*

Overall, the mechanism for the salinity IOD in the east EIO is similar to that for the biological IOD. In the east IOD zone, the stronger upwelling-favorable southeast winds along the west Sumatra coast in a p-IOD event not only shoaled the thermocline, but also brought low-temperature, high-nutrient and high-salinity waters to the upper layer.

The upwelling and the advection of the upwelling water defined the SST drop, enhanced biological activity, and elevated salinity in the east IOD zone during the p-IOD event.

Salinity in the water column especially SSS can be affected by the P-E in the east IOD (Fig. 6e and g). However, there was no significant SSS enhancement in comparison to salinity in the water column. This implies that the ocean processes, e.g., upwelling, entrainment and advection of the upwelling water were the dominant drivers for the enhanced salinity in the east IOD zone for the p-IOD event. The less contribution of the P-E to the salinity change could be attributed to the thick mixed-layer, and strong wind-driven upwelling, mixing and entrainment in the east IOD zone.

In the west IOD zone, the deepening of thermocline driven by the downwelling and surface water convergence (Fig. 6b) at station B not only led to the salinity drop in the upper 50–70 m, but also triggered the enhanced SST and decreased Chl-a in this region (Shi & Wang, 2021, 2022b). Unlike its contribution to salinity at station A in the east IOD zone, the P-E at station B played an important role on the salinity change especially the SSS variability in the 2019 p-IOD event. The significantly low salinity at the surface 5–10 m mixed-layer was attributed to the anomalously high P-E at station B in this period. This also suggests that the spatial patterns in the west IOD zone for the SSS anomaly (Fig. 1d), SST anomaly, and Chl-a anomaly (Shi & Wang, 2021, 2022b, 2024) could be different. It also shows that the ocean and atmospheric processes that drive the changes for salinity, temperature, and biological variability during the p-IOD event are not the same.

In this study, the in situ measurements at stations A and B only covered the 2019 p-IOD event. For the n-IOD event in 2022, SSS changes in the east and west IOD zones were opposite to the SSS change in the p-IOD in 2019 as characterized in Figs. 1–3. The 2022 n-IOD started with the weaker southeasterly wind along the west Sumatra coast from monthly surface wind data (Kalnay et al., 1996). The NCEP Global Ocean Data Assimilation System (GODAS) (Behringer et al., 1998; Ravichandran et al., 2013) shows that the 20 °C isothermal depth deepened about 20 m for most of the east IOD zone and shoaled 20–40 m in the west IOD zone (results not shown). The ocean dynamics in the east and west IOD zones provides further evidence that the reverse ocean processes drove the negative salinity IOD during the 2022 n-IOD event. It is also noted that the role of P-E cannot be assessed for the 2022 n-IOD event due to the lack of data availability.

4. Discussion

In this study, we use the 2019 p-IOD and 2022 n-IOD events as examples to demonstrate the salinity IOD as another facet for the IOD phenomenon. However, the salinity IOD is indeed a general feature and an indispensable facet of the IOD phenomenon. In fact, the salinity IOD is caused by the same ocean processes that also drive the SST IOD and biological IOD. The atmosphere process, i.e., P-E further enhanced the salinity IOD phenomenon especially for SSS of both the p-IOD and n-IOD events. During the study period, EIO also experienced other IOD events, e.g., moderate p-IOD in 2015 (Zhang et al., 2018) and severe n-IOD event in 2016 (Lu et al., 2018; Zhang et al., 2018). Fig. 2d shows that the DMI and BDMI reached +0.480 °C and +0.38 in the 2015 p-IOD event, while they were at −0.75 °C and −0.31 in the 2016 n-IOD event, respectively. On the other hand, the SDMI (Fig. 2c) reached +0.40 psu and −0.38 psu in the 2015 p-IOD and 2016 n-IOD event, respectively.

Fig. 7 provides the details of the salinity IOD (Fig. 7a and b), biological IOD (Fig. 7c and d), and SST IOD (Fig. 7e and f) in September 2015 (p-IO) and July 2016 (n-IOD). As quantified in Fig. 2c and d, the salinity IOD, biological IOD, and SST IOD indeed occurred in the two IOD zones with enhanced SSS, Chl-a, and depressed SST in the east IOD zone, compared to decreased SSS, Chl-a, and enhanced SST in the west IOD zone (Fig. 7a, c, e) in the 2015 p-IOD event. On the other hand, the decreased SSS, Chl-a, and elevated SST in the east IOD zone, compared to the enhanced SSS, Chl-a, and decreased SST in the west IOD zone (Fig. 7b, d, f) were found during the 2016 n-IOD event. It is also noted that the spatial patterns of the SSS anomaly and Chl-a ratio were co-located for a large portion of these two IOD zones. This indeed suggests that the ocean processes for the salinity IOD and biological IOD are the same even though the precipitation and evaporation could cause the difference in some regions.

In this work, we used the in situ measurements at stations A and B to better understand the subsurface dynamics of salinity, temperature, and

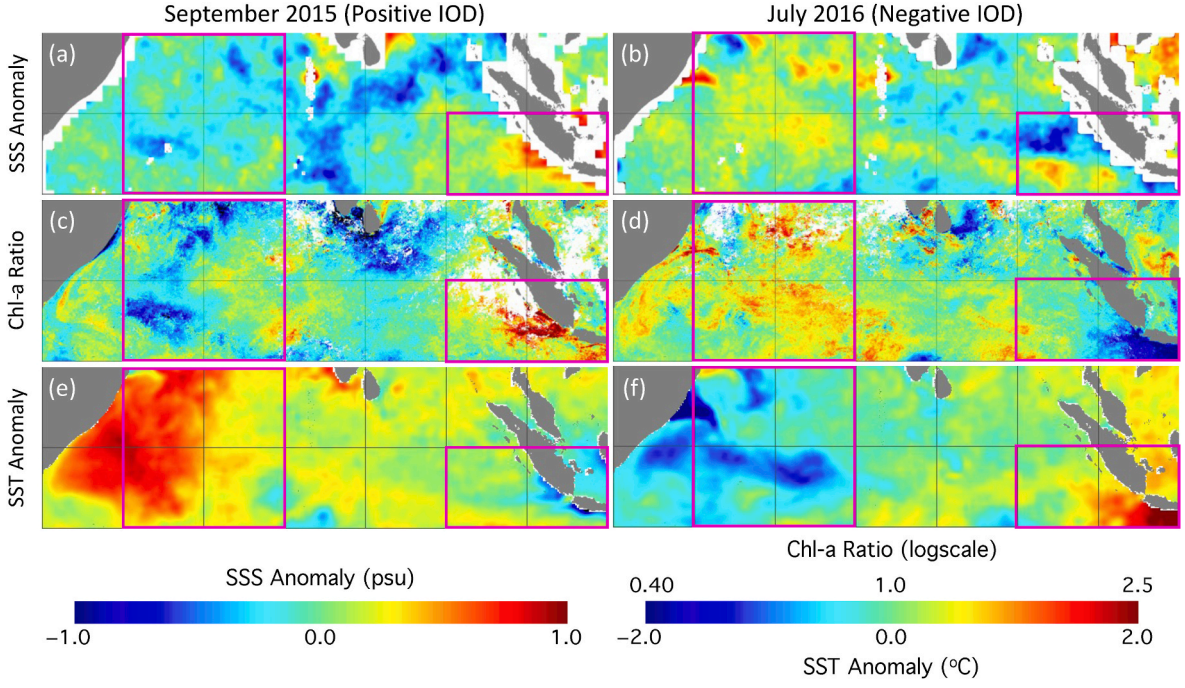

Fig. 7. Maps of the parameters in September 2015 for the p-IOD and July 2016 for the n-IOD for (a and b) SSS anomaly, (c and d) Chl-a anomaly (in ratio), and (e and f) SST anomaly.

the driving mechanisms in the two IOD zones. Further analyses of the WOA18 show that the mean profiles of salinity at the east (or west) IOD zone and the climatological salinity profiles at station A (or B) are similar to each other in terms of the vertical profile curvature shapes, halocline depth, etc., even though SSS values at the east (or west) IOD zone and the climatological salinity SSS at station A (or B) show some differences. On the other hand, the temporal variability of satellite SSS also shows that SSS at station A (or B) and the mean SSS for the entire east (west) IOD zone are similar. Previous studies have already showed that the driving forces at each station and their corresponding IOD zone are the same (Saji and Yamagata, 2003; Shi & Wang, 2021, 2024; Vinayachandran et al., 2002). Overall, the in situ measurements at stations A and B are good representatives for the east and west IOD zones, respectively, even though the spatial SSS variability may exist within each IOD zone.

It is noted that both the region and the driving forcing for the SSS IOD are different from numerous previous studies (Durand et al., 2013; Kido et al., 2019; Li et al., 2016; Sun et al., 2022a; Thompson et al., 2006; Zhang et al., 2016). In those studies, the domain of the west SSS IOD pole is either located in the central tropical Indian Ocean (Durand et al., 2013; Kido et al., 2019; Li et al., 2016; Zhang et al., 2016) or southern tropical Indian Ocean (Sun et al., 2022a), which are different from the well-defined west IOD zone for SST-based DMI and Chl-a-based BDMI (Saji et al., 1999; Shi and Wang, 2022b). Even though the SSS anomaly in the central tropical Indian Ocean indeed agree with those from the previous studies as shown in Fig. 1, the west SSS IOD pole we proposed in this study is in the west tropical Indian Ocean, which is consistent with the well-accepted definition of west pole of the IOD or BIOD phenomena from SST or Chl-a (Saji et al., 1999; Shi & Wang, 2021, 2022b; Webster et al., 1999).

Most importantly, the major driving forcings for the SSS anomaly described in the previous studies and in this work are significantly different. The previous studies showed that the SSS anomaly in the central tropical Indian Ocean was attributed to the westward advection of the Bay of Bengal water (Durand et al., 2013; Kido et al., 2019; Li et al., 2016; Thompson et al., 2006; Zhang et al., 2016). In comparison, in this study we show that the driving forcing for the west pole of SSS IOD is the precipitation-evaporation as well as thermocline dynamics due to the ocean processes such as Ekman pumping, Rossby wave propagation. In addition, it should be noted that the ocean processes in the east pole of the SSS IOD is the same as those for the SST and Chl-a IODs (Shi & Wang, 2021, 2024; Vinayachandran et al., 2002).

Furthermore, the NCEP Global Ocean Data Assimilation System (GODAS) (Behringer and Xue, 2004; Derber and Rosati, 1989) shows close connections among the Chl-a variability, SST, SSS, and 20 °C isothermal depth, and subsurface vertical velocity for the positive and negative BIOD events in 2019 and 2022, respectively (Shi and Wang, 2024). Shoaling thermocline in the east IOD zone and deepening thermocline in the west IOD zone were found in the 2019 p-IOD, and vice versa in the 2022 n-IOD event. These provide further evidence that the ocean processes in the west IOD zone as proposed in this study is different from the advection of low-salinity water for the salinity anomaly in the central tropical Indian Ocean reported in the other studies.

5. Conclusion

In this study, satellite-measured SSS showed the dipolar variability of SSS in the east and west EIO regions during the 2019 p-IOD and 2022 n-IOD events. The salinity IOD event as proposed in this study is different from the previous studies in terms of both the domain of the SSS dipolar pole and the driving forcing for the SSS anomaly during the IOD event.

The temporal variation in the difference of the average SSS anomalies in the east and west IOD zones is consistent with those of the DMI and BDMI indices. This demonstrates that the IOD event is not only a traditional SST phenomenon in the EIO, but also comprehensive activities involving many ocean parameters. In addition to recently reported BIOD (Shi & Wang, 2021, 2022b) accompanying with the SST IOD, the salinity IOD is another facet of the IOD phenomenon.

Using the in situ measurements in the east and west IOD zones, we show that the wind-driven upwelling and advection of the upwelling water were responsible for the enhanced salinity in the east IOD during the p-IOD and vice versa for the n-IOD. Both the ocean processes and the P-E are the driving forcings for the SSS anomalies during the IOD events in the west IOD zone. The increase of the salinity was found as deep as ~70–80 m during the 2019 p-IOD event. This is attributed to the ocean processes. In contrast to the ocean processes in the east IOD zone, the salinity anomaly in the surface 5–10 m during the IOD event was mainly caused by the anomalous P-E in the region. The contribution of the anomalously negative P-E to the salinity change at the halocline depth during the p-IOD is less significant.

In the west IOD zone, the driving forcing for the salinity variability is not exactly the same as those for the SST and biological IOD. The deepening of the 20 °C isotherm due to the downwelling and surface water convergence led to the drop of salinity in the water column during the 2019 p-IOD event. However, excessive P-E in the west IOD zone also played an important role for the drop of salinity especially SSS during the 2019 p-IOD event.

CRediT authorship contribution statement

Wei Shi: Writing – original draft, Investigation, Formal analysis, Conceptualization. **Menghua Wang:** Writing – review & editing, Project administration, Funding acquisition.

Declaration of competing interest

The authors declare that they have no known competing financial interests or personal relationships that could have appeared to influence the work reported in this paper.

Acknowledgements

This research was supported by the Joint Polar Satellite System (JPSS) funding. Figs. 1, 3 and 4 were produced using the Ocean Color Data Analysis and Processing System (OCDAPS) (https://doi.org/10.1117/12.2070478) developed by the NOAA Ocean Color Science Team. We thank two anonymous reviewers for their useful comments. The scientific results and conclusions, as well as any views or opinions expressed herein, are those of the author(s) and do not necessarily reflect those of NOAA or the Department of Commerce.

Data availability

Data will be made available on request.

References

Abram, N.J., Gagan, M.K., McCulloch, M.T., Chappell, J., Hantoro, W.S., 2003. Coral reef death during the 1997 Indian Ocean dipole linked to Indonesian wildfires. Science 301, 952–955. https://doi.org/10.1126/science.1083841.

Ashok, K., Guan, Z.Y., Yamagata, T., 2001. Impact of the Indian Ocean Dipole on the relationship between the Indian monsoon rainfall and ENSO. Geophys. Res. Lett. 28, 4499–4502. https://doi.org/10.1029/2001gl013294.

Behera, S.K., Yamagata, T., 2003. Influence of the Indian Ocean Dipole on the southern oscillation. J. Meteorol. Soc. Jpn. 81, 169–177. https://doi.org/10.2151/jmsj.81.169.

Behringer, D.W., Ji, M., Leetmaa, A., 1998. An improved coupled model for ENSO prediction and implications for ocean initialization. Part I: the Ocean Data Assimilation System. Mon. Weather Rev. 126, 1013–1021. https://doi.org/10.1175/1520-0493(1998)126<1013:Aicmfe>2.0.Co;2.

Behringer, D.W., Xue, Y., 2004. Evaluation of the global ocean data assimilation system at NCEP: the Pacific Ocean. Eighth Symposium on Integrated Observing and Assimilation Systems for Atmosphere, Oceans, and Land Surface AMS 84th Annual Meeting. Seattle, Washington.

Black, E., Slingo, J., Sperber, K.R., 2003. An observational study of the relationship between excessively strong short rains in coastal East Africa and Indian Ocean SST. Mon. Weather Rev. 131, 74–94. https://doi.org/10.1175/1520-0493(2003)131<0074:Aosotr>2.0.Co;2.

Boyer, T., Levitus, S., Garcia, H., Locarnini, R.A., Stephens, C., Antonov, J., 2005. Objective analyses of annual, seasonal, and monthly temperature and salinity for the world ocean on a 0.25 degrees grid. Int. J. Climatol. 25, 931–945. https://doi.org/10.1002/joc.1173.

Cai, W., Cowan, T., Raupach, M., 2009. Positive Indian Ocean Dipole events precondition southeast Australia bushfires. Geophys. Res. Lett. 36. https://doi.org/10.1029/2009gl039902.

Cai, W.J., Santoso, A., Wang, G.J., Weller, E., Wu, L.X., Ashok, K., Masumoto, Y., Yamagata, T., 2014. Increased frequency of extreme Indian Ocean Dipole events due to greenhouse warming. Nature 510, 254. https://doi.org/10.1038/nature13327.

Currie, J.C., Lengaigne, M., Vialard, J., Kaplan, D.M., Aumont, O., Naqvi, S.W.A., Maury, O., 2013. Indian Ocean Dipole and El nino/southern oscillation impacts on regional chlorophyll anomalies in the Indian Ocean. Biogeosciences 10, 6677–6698. https://doi.org/10.5194/bg-10-6677-2013.

Derber, J., Rosati, A., 1989. A global oceanic data assimilation system. J. Phys. Oceanogr. 19, 1333–1347. https://doi.org/10.1175/1520-0485(1989)019<1333:Agodas>2.0.Co;2.

Doi, T., Behera, S.K., Yamagata, T., 2020. Predictability of the super IOD event in 2019 and its link with El nino modoki. Geophys. Res. Lett. 47. https://doi.org/10.1029/2019GL086713.

Durand, F., Alory, G., Dussin, R., Reul, N., 2013. SMOS reveals the signature of Indian Ocean Dipole events. Ocean Dynam. 63, 1203–1212. https://doi.org/10.1007/s10236-013-0660-y.

Feng, M., Meyers, G., Wijffels, S., 2001. Interannual upper ocean variability in the tropical Indian Ocean. Geophys. Res. Lett. 28, 4151–4154. https://doi.org/10.1029/2001gl013475.

Fore, A.G., Yueh, S.H., Tang, W.Q., Stiles, B.W., Hayashi, A.K., 2016. Combined active/passive retrievals of ocean vector wind and sea surface salinity with SMAP. IEEE Trans. Geosci. Rem. Sens. 54, 7396–7404. https://doi.org/10.1109/Tgrs.2016.2601486.

Gao, L.B., Yu, W.D., Li, T., Adi, T.R., Budi, S., Triyono, Salvienty, M., 2014. Rainfall asymmetry in the southeast Indian Ocean between positive and negative IODs and its local impact. Atmos. Sci. Lett. 15, 127–133. https://doi.org/10.1002/asl2.479.

Goldberg, M.D., Kilcoyne, H., Cikanek, H., Mehta, A., 2013. Joint Polar Satellite System: the United States next generation civilian polar-orbiting environmental satellite system. J. Geophys. Res. Atmos. 118, 13463–13475. https://doi.org/10.1002/2013jd020389.

Iskandar, I., Rao, S.A., Tozuka, T., 2009. Chlorophyll-a bloom along the southern coasts of Java and Sumatra during 2006. Int. J. Rem. Sens. 30, 663–671. https://doi.org/10.1080/01431160802372309.

Kalnay, E., Kanamitsu, M., Kistler, R., Collins, W., Deaven, D., Gandin, L., Iredell, M., Saha, S., White, G., Woollen, J., Zhu, Y., Chelliah, M., Ebisuzaki, W., Higgins, W., Janowiak, J., Mo, K.C., Ropelewski, C., Wang, J., Leetmaa, A., Reynolds, R., Jenne, R., Joseph, D., 1996. The NCEP/NCAR 40-year reanalysis project. Bull. Am. Meteorol. Soc. 77, 437–471. https://doi.org/10.1175/1520-0477(1996)077<0437:Tnyrp>2.0.Co;2.

Kido, S., Tozuka, T., Han, W.Q., 2019. Anatomy of salinity anomalies associated with the positive Indian Ocean Dipole. J. Geophys. Res. Oceans 124, 8116–8139. https://doi.org/10.1029/2019jc015163.

Le Vine, D.A., Lagerloef, G.S.E., Colomb, F.R., Yueh, S.H., Pellerano, F.A., 2007. Aquarius: an instrument to monitor sea surface salinity from space. IEEE Trans. Geosci. Rem. Sens. 45, 2040–2050. https://doi.org/10.1109/Tgrs.2007.898092.

Li, J.D., Liang, C.J., Tang, Y.M., Dong, C.M., Chen, D.K., Liu, X.H., Jin, W.F., 2016. A new dipole index of the salinity anomalies of the tropical Indian Ocean. Sci. Rep. 6. https://doi.org/10.1038/srep24260.

Liu, X., Wang, M., 2018. Gap filling of missing data for VIIRS Global Ocean Color products using the DINEOF method. IEEE Trans. Geosci. Rem. Sens. 56, 4464–4476. https://doi.org/10.1109/Tgrs.2018.2820423.

Liu, X., Wang, M., 2019. Filling the gaps of missing data in the merged VIIRS SNPP/NOAA-20 Ocean Color product using the DINEOF method. Rem. Sens. 11, 178. https://doi.org/10.3390/rs11020178.

Liu, X., Wang, M., 2022. Global daily gap-free ocean color products from multi-satellite measurements. Int. J. Appl. Earth Obs. Geoinf. 108, 102714. https://doi.org/10.1016/j.jag.2022.102714.

Lu, B., Ren, H.L., Scaife, A.A., Wu, J., Dunstone, N., Smith, D., Wan, J.H., Eade, R., MacLachlan, C., Gordon, M., 2018. An extreme negative Indian Ocean Dipole event in 2016: dynamics and predictability. Clim. Dynam. 51, 89–100. https://doi.org/10.1007/s00382-017-3908-2.

Luo, J.J., Zhang, R.C., Behera, S.K., Masumoto, Y., Jin, F.F., Lukas, R., Yamagata, T., 2010. Interaction between El nino and extreme Indian Ocean Dipole. J. Clim. 23, 726–742. https://doi.org/10.1175/2009jcli3104.1.

O'Neill, P., Entekhabi, D., Njoku, E., Kellogg, K., 2010. The nasa soil moisture active passive (smap) mission: overview. 2010. Ieee Int. Geosci. Rem. Sens. Symp. 3236–3239. https://doi.org/10.1109/Igarss.2010.5652291.

Prajeesh, A.G., Swapna, P., Krishnan, R., Ayantika, D.C., Sandeep, N., Manmeet, S., Aditi, M., Sandip, I., 2022. The Indian summer monsoon and Indian Ocean Dipole connection in the IITM Earth system model (IITM-ESM). Clim. Dynam. 58, 1877–1897. https://doi.org/10.1007/s00382-021-05999-z.

Qiu, Y., Cai, W.J., Li, L., Guo, X.G., 2012. Argo profiles variability of barrier layer in the tropical Indian Ocean and its relationship with the Indian Ocean Dipole. Geophys. Res. Lett. 39. https://doi.org/10.1029/2012gl051441.

Rao, S.A., Behera, S.K., Masumoto, Y., Yamagata, T., 2002. Interannual subsurface variability in the tropical Indian Ocean with a special emphasis on the Indian Ocean Dipole. Deep-Sea Research Part Ii-Topical Studies in Oceanography 49, 1549–1572. https://doi.org/10.1016/S0967-0645(01)00158-8.

Ratna, S.B., Cherchi, A., Osborn, T.J., Joshi, M., Uppara, U., 2021. The extreme positive Indian Ocean Dipole of 2019 and associated Indian summer monsoon rainfall response. Geophys. Res. Lett. 48. https://doi.org/10.1029/2020GL091497.

Ravichandran, M., Behringer, D., Sivareddy, S., Girishkumar, M.S., Chacko, N., Harikumar, R., 2013. Evaluation of the Global Ocean Data assimilation system at INCOIS: the tropical Indian Ocean. Ocean Model. 69, 123–135. https://doi.org/10.1016/j.ocemod.2013.05.003.

Rayner, N.A., Parker, D.E., Horton, E.B., Folland, C.K., Alexander, L.V., Rowell, D.P., Kent, E.C., Kaplan, A., 2003. Global analyses of sea surface temperature, sea ice, and night marine air temperature since the late nineteenth century. J. Geophys. Res. Atmos. 108. https://doi.org/10.1029/2002jd002670.

Saji, N.H., Goswami, B.N., Vinayachandran, P.N., Yamagata, T., 1999. A dipole mode in the tropical Indian Ocean. Nature 401, 360–363. https://doi.org/10.1038/43855.

Saji, N.H., Yamagata, T., 2003. Structure of SST and surface wind variability during Indian ocean dipole mode events: COADS observations. J. Clim. 16, 2735–2751. https://doi.org/10.1175/1520-0442(2003)016<2735:Sosasw>2.0.Co;2.

Shi, W., Wang, M., 2021. A biological Indian Ocean Dipole event in 2019. Sci. Rep. 11, 2452. https://doi.org/10.1038/s41598-021-81410-5.

Shi, W., Wang, M., 2022a. Phytoplankton biomass dynamics in the Arabian Sea from VIIRS observations. J. Mar. Syst. 227, 103670. https://doi.org/10.1016/j.jmarsys.2021.103670.

Shi, W., Wang, M., 2024. A negative biological Indian Ocean dipole event in 2022. Sci. Rep. 14, 1110. https://doi.org/10.1038/s41598-024-51347-6.

Shi, W., Wang, M.H., 2022b. Biological dipole mode indices: new parameters to characterize the physical and biological processes of the Indian Ocean Dipole event. Prog. Oceanogr. 206, 102847. https://doi.org/10.1016/j.pocean.2022.102847.

Sun, Q.W., Du, Y., Zhang, Y.H., Feng, M., Chowdary, J.S., Chi, J.W., Qiu, S., Yu, W.D., 2019. Evolution of sea surface salinity anomalies in the southwestern tropical Indian Ocean during 2010-2011 influenced by a negative IOD event. J. Geophys. Res. Oceans 124, 3428–3445. https://doi.org/10.1029/2018jc014580.

Sun, Q.W., Zhang, Y.H., Du, Y., Jiang, X.W., 2022a. Asymmetric response of sea surface salinity to extreme positive and negative Indian Ocean Dipole in the southern tropical Indian Ocean. J. Geophys. Res. Oceans 127. https://doi.org/10.1029/2022JC018986.

Sun, S.W., Fang, Y., Zu, Y.C., Liu, L., Li, K.P., 2022b. Increased occurrences of early Indian Ocean Dipole under global warming. Sci. Adv. 8. https://doi.org/10.1126/sciadv.add6025.

Thompson, B., Gnanaseelan, C., Salvekar, P.S., 2006. Variability in the Indian Ocean circulation and salinity and its impact on SST anomalies during dipole events. J. Mar. Res. 64, 853–880. https://doi.org/10.1357/002224006779698350.

Thushara, V., Vinayachandran, P.N., 2020. Unprecedented surface chlorophyll blooms in the southeastern arabian sea during an extreme negative Indian Ocean Dipole. Geophys. Res. Lett. 47. https://doi.org/10.1029/2019GL085026.

Ummenhofer, C.C., England, M.H., McIntosh, P.C., Meyers, G.A., Pook, M.J., Risbey, J.S., Gupta, A.S., Taschetto, A.S., 2009. What causes southeast Australia's worst droughts? Geophys. Res. Lett. 36. https://doi.org/10.1029/2008gl036801.

Vinayachandran, P.N., Iizuka, S., Yamagata, T., 2002. Indian Ocean dipole mode events in an ocean general circulation model. Deep-Sea Research Part Ii-Topical Studies in Oceanography 49, 1573–1596. https://doi.org/10.1016/S0967-0645(01)00157-6.

Vinayachandran, P.N., Nanjundiah, R.S., 2009. Indian Ocean sea surface salinity variations in a coupled model. Clim. Dynam. 33, 245–263. https://doi.org/10.1007/s00382-008-0511-6.

Vinayachandran, P.N., Saji, N.H., Yamagata, T., 1999. Response of the Equatorial Indian Ocean to an unusual wind event during 1994. Geophys. Res. Lett. 26, 1613–1616. https://doi.org/10.1029/1999gl900179.

Wang, G.J., Cai, W.J., Santoso, A., Abram, N., Ng, B., Yang, K., Geng, T., Doi, T., Du, Y., Izumo, T., Ashok, K., Li, J.P., Li, T., Mckenna, S., Sun, S.W., Tozuka, T., Zheng, X.T., Liu, Y., Wu, L.X., Jia, F., Hu, S.J., Li, X.C., 2024. The Indian Ocean Dipole in a warming world. Nat. Rev. Earth Environ. 5, 588–604. https://doi.org/10.1038/s43017-024-00573-7.

Wang, M., Liu, X., Tan, L., Jiang, L., Son, S., Shi, W., Rausch, K., Voss, K., 2013. Impacts of VIIRS SDR performance on ocean color products. J. Geophys. Res. Atmos. 118, 10347–10360. https://doi.org/10.1002/Jgrd.50793.

Wang, M., Son, S., 2016. VIIRS-derived chlorophyll-a using the ocean color index method. Rem. Sens. Environ. 182, 141–149. https://doi.org/10.1016/j.rse.2016.05.001.

Webster, P.J., Moore, A.M., Loschnigg, J.P., Leben, R.R., 1999. Coupled ocean-atmosphere dynamics in the Indian Ocean during 1997-98. Nature 401, 356–360. https://doi.org/10.1038/43848.

Zhang, L., Han, W.Q., Hu, Z.Z., 2021. Interbasin and multiple-time-scale interactions in generating the 2019 extreme Indian Ocean Dipole. J. Clim. 34, 4553–4566. https://doi.org/10.1175/Jcli-D-20-0760.1.

Zhang, L.Y., Du, Y., Cai, W.J., 2018. Low-frequency variability and the unusual Indian Ocean Dipole events in 2015 and 2016. Geophys. Res. Lett. 45, 1040–1048. https://doi.org/10.1002/2017gl076003.

Zhang, Y.H., Du, Y., Qu, T.D., 2016. A sea surface salinity dipole mode in the tropical Indian Ocean. Clim. Dynam. 47, 2573–2585. https://doi.org/10.1007/s00382-016-2984-z.

Zhang, Y.H., Du, Y., Zheng, S.J., Yang, Y.L., Cheng, X.H., 2013. Impact of Indian Ocean Dipole on the salinity budget in the equatorial Indian Ocean. J. Geophys. Res. Oceans 118, 4911–4923. https://doi.org/10.1002/jgrc.20392.

Zubair, L., Rao, S.A., Yamagata, T., 2003. Modulation of Sri Lankan maha rainfall by the Indian Ocean Dipole. Geophys. Res. Lett. 30. https://doi.org/10.1029/2002gl015639.